Synthesis and characterization of AsO[(W,Mo)O$_3$]$_{13}$, a new (6)-intergrowth tungsten bronze (ITB)

Meriem Goudjil [a,d,*], Giovanni Orazio Lepore [a], Luca Bindi [a,b], Enrico Mugnaioli [c], Tommaso Baroni [a], Djillali Mezaoui [d], Paola Bonazzi [a]

[a] Dipartimento di Scienze della Terra, Università degli Studi di Firenze, via G. La Pira 4, I-50121, Firenze, Italy
[b] CNR-Istituto di Geoscienze e Georisorse, Sez. di Firenze, via G. La Pira 4, I-50121, Firenze, Italy
[c] Dipartimento di Scienze della Terra, Università degli Studi di Pisa, Via S. Maria 53, I-56126, Pisa, Italy
[d] Laboratoire des Sciences des Matériaux (LSM), Université des Sciences et de la Technologie Houari Boumediène, Alger, 16111, Algeria

ARTICLE INFO

ABSTRACT

Crystals of a new arsenic tungsten-molybdenum oxide, AsO[(W,Mo)O$_3$]$_{13}$, have been grown through vapour phase transport at high temperature (1123 K). The crystal structure was investigated by combining electron and single-crystal X-ray diffraction techniques, electron microprobe chemical analysis and X-ray absorption spectroscopy. Single-crystal XRD yielded the orthorhombic unit-cell parameters $a = 25.0895$, $b = 7.3061$, $c = 3.9089$ Å. Although electron diffraction indicated a doubled translation along [001], superstructure reflections were undetectable with X-ray diffraction so that only the average structure (sub-cell) was determined. The most reliable structural model was obtained in the $P222$ space group ($R_1 = 6.96\%$). It exhibits an octahedral framework which forms six-octahedra thick perovskite slabs (PTB) alternated to single hexagonal tungsten bronze (HTB) modules, indicating that the compound corresponds to a (6)-ITB phase. As^{3+} was found to be disordered on two off-centred, symmetry-related sites into the hexagonal channels with the typical pyramidal AsO$_3$ geometry. This is in agreement with the results of the extended X-ray absorption fine structure that indicate an As–O bond distance of 1.77 Å. The ordered distribution of As within the tunnels, likely related to the doubling of periodicity along [001], could not be determined.

1. Introduction

Tungsten bronze oxides (TBOs) are a large group of non-stoichiometric compounds with general formula A_xWO_3 ($0 < x \leq 1$), where A is a mono-, di-, or tri-valent cation hosted in the open cavities of three-dimensional frameworks built upon corner-sharing of WO$_6$ octahedral units. In the last decades they have been extensively investigated for their peculiar structures, compositional variability, and potential applications. TBOs are recently gaining increasing interest as functional materials for different applications: in catalytic reactions [1–5], in optoelectronic devices [6], as electrodes in supercapacitors [7,8], and for the production of energy-saving window glasses [9–11].

Until 1953, only three structural types of the TBOs were known: the perovskite (PTB) [12], the tetragonal (TTB) [13,14] and the hexagonal (HTB) tungsten bronzes [15,16]. The fourth type, discovered only later [17], can be considered as a merge of two of the aforementioned structural types (PTB and HTB) and therefore named intergrowth tungsten bronze (ITB).

In comparison to the other types of TBOs, ITB structures show a greater structural variability related to different sequences of PTB and HTB modules leading to a larger variety of chemical elements which can be accommodated. Hussain et al. [17,18] proposed a convenient designation to classify the ITB structures into three main categories, denoted as follows: (*i*) (*n*)-ITB (observed for $n = 2, 3, 4, 5, 6, 7, 8, 9, 10$ and 11 [17, 19–24]) when a single HTB slab alternates with PTB slabs of n rows of MO$_6$ octahedra (M: W, Mo, Nb, etc.); (*ii*) (1,*n*)-ITB (obtained with $2 \leq n \leq 14$ [25–29]) when the HTB module is double, *i.e.*, comprises two rows of hexagonal tunnels; (*iii*) (1,1,*n*)-ITB (obtained with $3 \leq n \leq 7$ [30,31]) when the HTB module includes three rows of hexagonal tunnels. Indeed, more notations are possible. Following the same reasoning, ITB structures containing four or five rows of hexagonal tunnels [25] have to be denoted as (1,1,1,*n*)- or (1,1,1,1,*n*)-ITB phases, respectively.

A study on a series of several (*n*)-ITB molybdenum-bronze oxides, with $2 \leq n \leq 5$ and As^{3+} located in off-center positions inside the

---

Table 1
EMPA data for the (6)-ITB compound.

	Avg. 4 point analyses (wt.%)	Range
WO_3	69.78	68.98–70.20
MoO_3	26.97	26.69–27.65
As_2O_3	3.40	3.36–3.45
Total	100.15	100.05–100.35
Norm. (Mo + W) = 13		
W	8.01	
Mo	4.99	
As	0.91	

Table 2
Crystallographic data, experimental details and structure refinement parameters for the (6)-ITB compound $AsO(W_{0.62}Mo_{0.38}O_3)_{13}$.

Crystal data	
Chemical formula	$AsO(W_{0.62}Mo_{0.38}O_3)_{13}$
Crystal system, space group	Orthorhombic, $P222$ (#16)
Temperature (K)	293
a, b, c (Å)	25.0895(17), 7.3061(4), 3.9089(3)
V (Å^3)	716.53(8)
Z	1
Radiation type	MoK_a ($\lambda = 0.71073$ Å)
Crystal size (mm)	$0.04 \times 0.03 \times 0.02$
Data collection	
Diffractometer	Oxford Diffraction Xcalibur 3
Absorption correction	Multi-scan
No. of measured, independent and observed $[I > 2\sigma(I)]$ reflections	8116, 2517, 1476
R_{int}	0.071
$(\sin\theta/\lambda)_{max}$ (Å^{-1})	0.765
Refinement	
$R[F^2 > 2\sigma(F^2)]$, w$R(F^2)$, S	0.070, 0.205, 1.04
No. of parameters	79
No. of restraints	0
$\Delta\rho_{max}, \Delta\rho_{min}$ (e Å^{-3})	+11.7, −6.8

Table 3
Fractional atomic coordinates and isotropic (*) or equivalent isotropic displacement parameters (Å^2) in the structure of the (6)-ITB compound.

Site	x	y	z	U_{eq}/U_{iso}
M1	0.07335(4)	0.2507(2)	0.4243(3)	0.0108(3)
M2	0.22044(4)	0.2476(2)	0.5743(3)	0.0104(3)
M3	0.36865(4)	0.2540(2)	0.4278(3)	0.0091(3)
M4	½	0	½	0.067(2)
As	½	0.390(1)	½	0.044(4)
O1	0.239(1)	0	½	0.04(1)*
O2	0.2994(8)	0.298(3)	0.486(5)	0.021(5)*
O3	0.2236(9)	0.252(3)	0.008(7)	0.037(6)*
O4	0	0.289(4)	½	0.023(7)*
O5	0.3728(8)	0.245(3)	0.986(5)	0.030(5)*
O6	½	0	0	0.03(1)*
O7	0.393(1)	½	½	0.016(6)*
O8	0.0739(7)	0.249(3)	0.990(7)	0.035(6)*
O9	0.1497(7)	0.209(3)	0.503(5)	0.024(5)*
O10	0.4490(8)	0.185(3)	0.503(6)	0.025(5)*
O11	0.363(1)	0	½	0.029(8)*
O12	0.088(2)	½	½	0.05(1)*
O13	0.212(2)	½	½	0.07(1)*
O14	0.063(2)	0	½	0.07(1)*
O15	½	0.43(1)	½	0.10(3)*

Note: s.o.f. are the following: M sites = 0.62 W + 0.38 Mo; As = 0.50 As + 0.50 □; O15 = 0.50 O +0.50 □

hexagonal tunnels, was recently reported [24]. In the ensuing search of new ITB phases in the As–W–Mo–O system, we recently obtained a new compound, likely belonging to the ITB family, as inferred from a comparison of its unit-cell and those of the (n)-ITB previously studied (*e.g.* Zakharov et al. [32], Iglesias et al. [33], Klingstedt et al. [34]). In particular, analogies with the unit cell reported by Steadman et al. [19] for the orthorhombic $Sn_4W_{24}O_{76}$ compound, which was described in its basic structural pattern and shows six-octahedra thick slabs, hinted at a possible synthesis of a (6)-ITB structure, a member of the ITB family lacking a full structural characterization.

To increase the knowledge of the (n)-ITB family, a structural study of this compound was carried out combining X-ray and electron diffraction data with electron microprobe analysis and X-ray absorption spectroscopy.

2. Materials and experimental methods

2.1. Synthesis and sample identification

As_2O_3 (99.5%, Sigma-Aldrich), MoO_3 (99.5%, Fluka), WO_3 (99.99%, Sigma-Aldrich) and W-metallic powder (99.9%, Alfa Aesar) were mixed, in equimolar ratios, ground in an agate mortar and then charged in a quartz ampoule to be torch-sealed under vacuum (base pressure $P = 10^{-4}$ mbar). Crystals of the studied compound were grown through vapour phase transport (VPT) method. The sealed tube (5 and 100 mm in diameter and length, respectively) was placed in a horizontal two-zone tubular furnace, heated initially at $T = 873$ K, and left for 12 h. Subsequently, the temperature of the furnace was increased at the rate of 50 K/h and kept for a week at $T = 1123$ K, which fits the temperature range (1073−1223 K) where the ITB compounds with W component are observed to form. After the synthesis took place, the temperature of the furnace was slowly decreased, cooled at 10 K/h down to $T = 673$ K followed by quenching at room temperature.

From the bottom of the reaction tube, two types of crystal (black and violet in colour) were recovered. The chemical composition of both black and violet crystals was preliminarily assessed on unpolished crystal fragments by SEM/EDS using a ZEISS EVO MA15 scanning electron microscope equipped with an Oxford ULTIM MAX 40 mm^2 EDS detector, operating with an accelerating voltage of 15 kV and a current of 0.7 nA. The EDS spectra indicate that the same elements (As, W, Mo and O) characterize the two phases, but with different relative amounts; in particular, the W/Mo ratio is higher in the black crystals. SEM images of the two types of crystals are shown in Fig. S1 (see supporting information file).

Unit-cell parameters for both types of crystals were determined using a Bruker D8 Venture diffractometer equipped with a Photon II CCD detector and graphite-monochromatized Mo $K\alpha$ radiation. Unit-cell parameters for violet crystals are $a = 20.27$, $b = 7.20$, $c = 3.99$ Å, $\alpha = \beta = \gamma = 90°$, quite similar to those found for $(AsO)(MoO_3)_5$ [24] and thus indicating a (2)-ITB structure. On the other hand, the measured cell dimensions for the black crystal are $a = 25.12$, $b = 7.32$ and $c = 3.91$ Å, $\alpha = \beta = \gamma = 90°$, thus pointing to a likely new (6)-ITB phase. For this reason, the following experimental techniques and relative results deal with this phase only.

The occurrence of two ITB structural types in the bulk sample is also verified through powder diffraction analysis, see Fig. S2.

2.2. Electron microprobe analysis

Chemical composition was carried on selected crystals embedded in epoxy resin, polished with diamond paste down to 0.25 μm and then coated with a ~28 nm-thick graphite layer using a JEOL-JXA-8230 WD-ED electron-probe microanalyzer (EMPA). Operating conditions were as follows: 20 kV accelerating potential, 50 nA beam current, 1 μm beam diameter and 15 s as counting time for each element. The quantitative analysis was performed on the basis of intensity measurements of $L_{\alpha1}$ X-ray emission lines of W, Mo and As. W, Mo and GaAs were used as standards. Raw data were corrected for matrix effects using the ΦρZ

Table 4
EXAFS multiparameter fit details.

	Sample	S_0^2	N	R (Å)	σ^2 (Å²)	ΔE_0	D.T. (K)
As–O	Arsenolite	0.8(1)	3	1.79(1)	0.002(1)	2.9(1.4)	240(18)/276(19)
As–O	(6)-ITB	0.9(1)	3	1.77(2)	0.0010(5)	2.9	

Notes: S_0^2 = Many Body amplitude reduction factor, N = path degeneracy, R = path length, σ^2 = Debye-Waller factor, $D.T$ = Debye Temperature. Interatomic distances for arsenolite shells higher than the first one vary within 0.01 Å (relative value) with respect to the model of Ballirano and Maras [46].
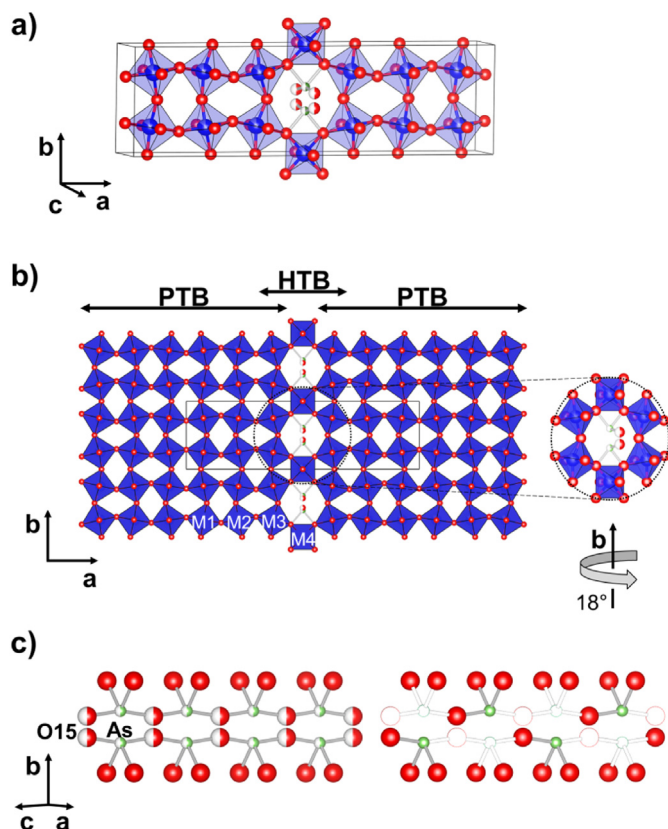

Fig. 1. Polyhedral representation of **(a)** unit-cell structure and **(b)** structural model of the (6)-ITB $AsO[(W,Mo)O_3]_{13}$ compound down [001]. Oxygen atoms are drawn as red circles, and the partially occupied As and O15 are depicted in green/white and red/white, respectively. MO_6 octahedra are given in blue. The enlarged circular view (right) shows the hexagonal channel where As adopts the typical pyramidal geometry. **(c)** Detail of the As–O configuration inside the channel (view down [104]): average configuration (left) and possible ordering scheme (right).

method of the JEOL series of programs. On the basis of 13 octahedral cations, the average chemical composition (Table 1), yields the formula $As_{0.91}W_{8.01}Mo_{4.99}O_{39}$.

2.3. X-ray diffraction study

X-ray data collection was carried out by means of an Oxford Diffraction Xcalibur 3 diffractometer equipped with a Sapphire 2 CCD detector on a minute black crystal. Intensity integration and standard Lorentz-polarization correction were performed with the *CrysAlis* RED [35] software package. The program ABSPACK in *CrysAlis* RED [35] was used for the absorption correction.

Unit-cell parameters are $a = 25.0895(17)$, $b = 7.3061(4)$, $c = 3.9089(3)$ Å; $\alpha = \beta = \gamma = 90.00°$. A total of 8116 reflections was merged in the *mmm* Laue class ($R_{int} = 0.071$). No systematic extinctions were observed. Attempts to solve the structure were then carried out in the *P222*, *Pmm2*, *Pm2m*, *P2mm* and *Pmmm* space groups by means of *SHELXS*

Table 5
Bond distances (Å) and distortion parameters in the structure of the (6)-ITB compound.

Atom—O	Bond distance (Å)	Atom—O	Bond distance (Å)
M1—O8	1.70(3)	M3—O5	1.73(2)
M1—O14	1.873(7)	M3—O2	1.78(2)
M1—O12	1.882(8)	M3—O11	1.882(3)
M1—O4	1.885(4)	M3—O7	1.922(9)
M1—O9	1.96(2)	M3—O10	2.10(2)
M1—O8	2.21(3)	M3—O5	2.18(2)
<M1—O>	1.920	<M3—O>	1.934
λ	1.024	λ	1.028
σ^2	61.7	σ^2	74.2
M2—O3	1.70(3)	M4—O10 (× 4)	1.86(2)
M2—O9	1.82(2)	M4—O6 (× 2)	1.9545(2)
M2—O13	1.877(5)	<M4—O>	1.892
M2—O1	1.893(9)	λ	1.002
M2—O2	2.04(2)	σ^2	3.7
M2—O3	2.21(3)		
<M2—O>	1.923	As—O10 (× 2)	1.97(2)
λ	1.028	As—O15	1.97(1)
σ^2	69.6		

Note: Distortion parameters (mean quadratic elongation λ and angular distortion σ^2) calculated according to Robinson et al. [48].

[36]. Despite the statistics on normalized structure factors indicated a centrosymmetric space group ($|E^2−1| = 1.23$), a reliable model was obtained in the *P222* space group. To check for possible higher symmetry, the ADDSYM algorithm in the PLATON program [37] was used. No additional symmetry with a plausible structural model was found.

Three independent metal sites (M1, M2, M3) were found at $4u$ and one (M4) at $1f$ Wyckoff position. The site occupancy factor (s.o.f.) at the octahedral M sites was refined using scattering curves (W vs. Mo) for neutral atoms taken from the International Tables for Crystallography [38]. Due to the high correlation values among occupancies of the four M sites a unique free variable for all the M sites was refined. The crystal was refined as a merohedral twin. Partially-occupied As site was found at the $2p$ Wyckoff position, 0.80 Å away from the two-fold symmetry axis along the [100] direction, suggesting a possible two-fold superstructure. Thus, the occupancy of As was fixed to 0.50. An anisotropic model was adopted for M and As while all the O atoms were kept isotropic ($R_1 = 6.99\%$ for 1476 reflections with $F_o > 4\sigma(F_o)$). The highest peaks on the ΔF map were observed at $\simeq 0.7$ Å from the M4 site. A further residual peak (Wyckoff: $2o$) was found and refined as half-occupied oxygen position, thus completing the As coordination. Attempts to refine the average structure in a lower symmetry (*i.e. P2* space group) did not lead to define the As ordering. Several crystals were then used to check for the presence of superstructure reflections but no reliable supercells were observed.

Details on data collection and refinement are reported in Table 2. Atomic coordinates and displacement parameters are given in Table 3. Further structural details are provided in the CIF available from the Cambridge Crystallographic Data Centre with CCDC number: 2232294.

2.4. Electron diffraction

To check the possible presence of superstructure reflections in the (6)-ITB phase a transmission electron microscopy study was carried out.
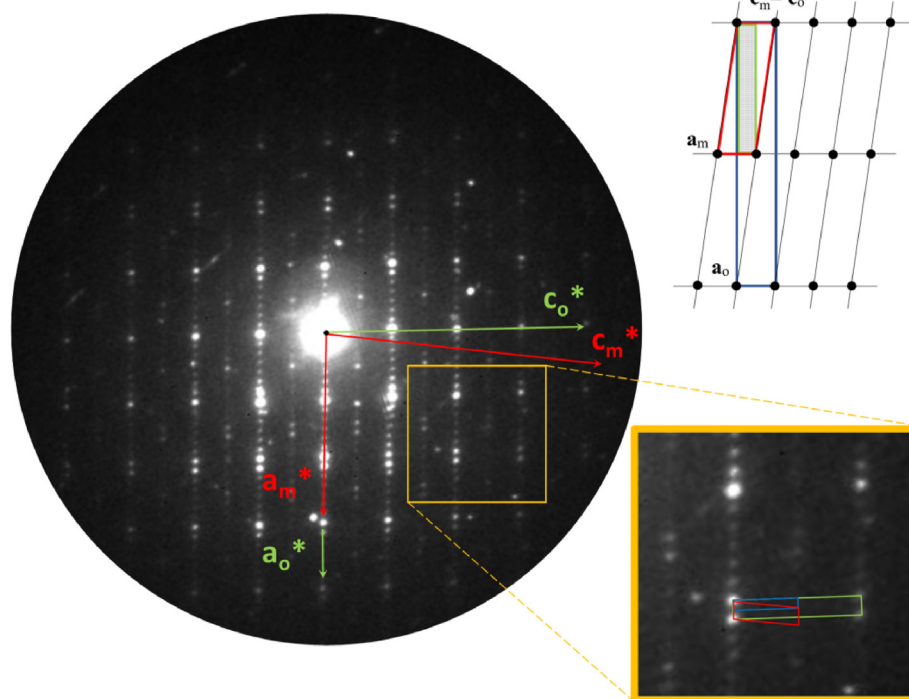
Fig. 2. SAED pattern oriented along [010] of an ordered domain of the AsO[(W,Mo)O$_3$]$_{13}$ compound. The sketch at the right-upper corner of the picture shows the different unit-cell choices (direct space) corresponding to those lined in the square detail (yellow lined) of the SAED pattern (reciprocal space): the *P* monoclinic ($a_m = 26.5$, $b_m = 7.3$, $c_m = 7.8$ Å and $b = 97.8°$, in red) and the *B*-centred orthorhombic, or pseudo-orthorhombic, ($a_o = 52.5$, $b_o = 7.3$ and $c_o = 7.8$ Å, in blue) supercells as observed by ED, together with the orthorhombic subcell ($a = 25.0895$, $b = 7.3061$, $c = 3.9089$ Å, in pale green) as determined by SC-XRD.

Few selected crystals were crushed between microscope glass slides and then transferred to a holey carbon-coated copper grid by gently rubbing the grid onto the surface of the glass substrate. The grains were analysed combining transmission electron microscopy (TEM), in-zone selected-area electron diffraction (SAED) and 3D electron diffraction (3D-ED) [39].

Conventional TEM, SAED and 3D-ED analyses were performed at room temperature with a JEOL JEM-F200 Multipurpose TEM, working at 200 kV and equipped with a Schottky field emission gun (FEG). TEM data were acquired by a Gatan RIO-16 CMOS camera. Diffraction data were recorded at room temperature by an ASI Cheetah hybrid-pixel detector working in sequential mode at 24bit. 3D-ED data were collected in sequential steps of 1°, with a nano-beam of about 40 nm obtained by inserting a 10 μm condenser aperture. The beam was precessed by a NanoMEGAS Topspin device, with a precession semi-angle kept at 1°. Exposure time for each 3D-ED pattern was 1 s. Camera length for both 3D-ED and SAED was 250 mm, equivalent in the direct space to a maximum resolution of about 0.75 Å. 3D-ED data were analysed using the software PETS2 [40].

SAED and 3D-ED revealed extra reflections that double the periodicity along the **c** axis, giving rise to a *B*-centred orthorhombic, or pseudo-orthorhombic, unit cell with $a = 52.5$, $b = 7.3$, $c = 7.8$ Å, $\alpha = \gamma = 90°$, $\beta \simeq 90.7°$. The corresponding primitive lattice results in a monoclinic unit cell with $a = 26.5$, $b = 7.3$, $c = 7.8$ Å and $\beta \simeq 97.8°$. Nevertheless, due to the high error in cell angle determination intrinsic to the technique as well as the presence of diffuse scattering which considerably affects reflection intensities, it was not possible to discriminate with confidence between monoclinic or orthorhombic symmetry.

2.5. X-ray absorption spectroscopy (XAS)

X-ray absorption near edge structure (XANES) and extended X-ray absorption fine structure (EXAFS) were carried out on a 1.3 cm pellet made of 50 mg of cellulose and *ca.* 7 mg of powder (sufficient to keep the total absorption $\mu < 1.5$ at both measured absorption edges) of (6)-ITB crystals selected under the optical microscope. The experiment was performed at BM08 "LISA" CRG beamline at the European Synchrotron Radiation Facility (ESRF) in Grenoble, France [41]. Data were collected at As *K*-edge (11866.7 eV) and W L_{III}-edge (10206.7 eV). The sample was measured at room temperature using a pair of Si (111) flat crystals. Higher harmonics rejection was obtained through Si coated collimating/focusing mirrors (with E_{cutoff} ~15 keV). Spectra of GaAs, metallic tungsten (W), arsenolite (As$_2$O$_3$) and tungsten trioxide (WO$_3$) were also measured for comparison.

Standard procedures for raw data treatment [42] and merge of multiple spectra were followed using the software ATHENA [43]. For the EXAFS fits of arsenolite and the (6)-ITB compound, model atomic clusters centred on the absorber atom were obtained by ATOMS [44]; theoretical amplitude and phase functions were generated using the FEFF8 code [45] starting from the coordinates reported by Ballirano and Maras [46]. EXAFS spectra were fitted through ARTEMIS [43] on the basis of the model of Ballirano and Maras [46] in the Fourier-Transform (FT) space [k range 3–14 Å^{-1} and 2.5–7.3 Å^{-1} for arsenolite and (6)-ITB, respectively]. Fit results are reported in Table 4. For arsenolite, coordination shells higher than the first one were satisfactorily fitted using two relative parameters for interatomic distances and the correlated Debye model [47] was used to compute the Debye-Waller factor for each path employing a total of two variables. EXAFS fit of As first coordination shell in the (6)-ITB compound was performed by fixing ΔE_0 to 2.9 eV, based on the results of arsenolite.

3. Results and discussion

The structural formula derived from the refinement, AsO(MO$_3$)$_{13}$ with M = (W$_{0.62}$Mo$_{0.38}$), well matches the chemical data (Table 1).

The model obtained exhibits an octahedral framework consisting of an alternation of single HTB modules and six octahedra-thick PTB slabs, thus confirming that the obtained W-rich oxide corresponds to a (6)-ITB phase (Fig. 1).

In detail, the PTB slabs are formed by three corner-sharing independent MO$_6$ octahedra. The M1, M2 and M3 cations are off-centred in the octahedra thus leading to high distortion parameters (σ^2: 61.7–74.2; λ: 1.024–1.028; Robinson et al. [48]). The HTB slab contains M4 (Wyckoff position: 1*f*), which lies in the equatorial centre of a more regular ($\sigma^2 = 3.7$, λ = 1.002) and smaller octahedron (see Table 5).

The As atom, exhibiting a high value of the displacement parameters

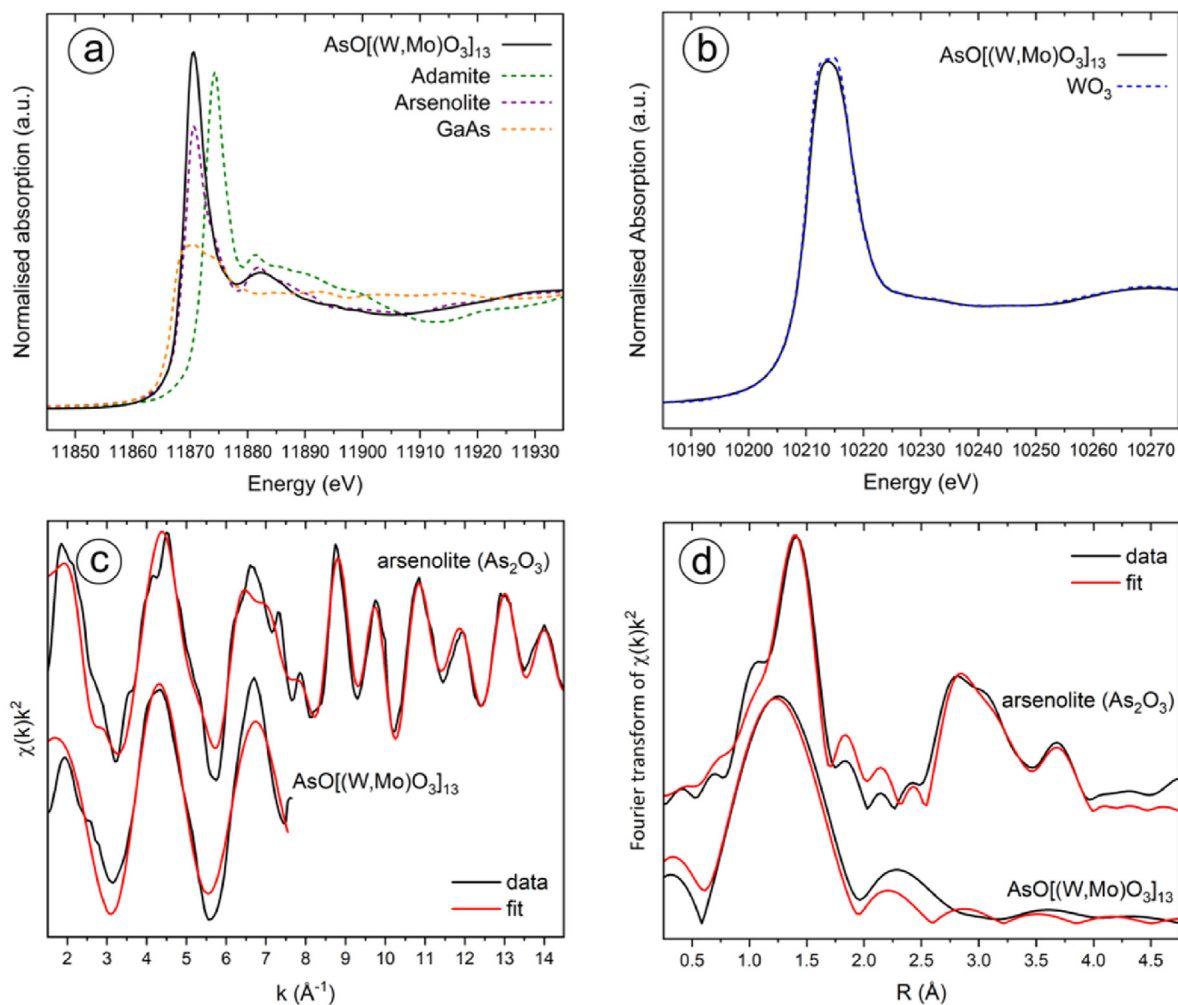**Fig. 3.** Normalized As K- **(a)** and W L_{III}-edge **(b)** XANES spectra of AsO[(W,Mo)O$_3$]$_{13}$ and model compounds; adamite data are taken from George et al. [51]. EXAFS **(c)** and EXAFS Fourier-Transform **(d)** of AsO[(W,Mo)O$_3$]$_{13}$ and arsenolite. Spectra were acquired in transmission mode with a fixed 5 eV step in the pre-edge region, 0.25 eV step around the edge and a k step of 0.05 Å^{-1}. The maximum k of 8 Å^{-1} for As K-edge spectra is due to the presence of W L_I edge at 12099.8 eV. The main As absorption edge of AsO[(W,Mo)O$_3$]$_{13}$ lies at energy values intermediate between those of adamite (As^{5+}) and GaAs, at the same value of arsenolite (As$_2$O$_3$) thus clearly indicating that As is present as As^{3+}. The W L_{III}-edges of AsO[(W,Mo)O$_3$]$_{13}$ and WO$_3$ lie at the same energy position, indicating that W in the sample is hexavalent.

Table 6
Bond valence sums for AsO[(W,Mo)O$_3$]$_{13}$.

	M1	M2	M3	M4	½As	$\sum$O
O1		1.01$^{\times 2\rightarrow}$				2.02
O2		0.66	1.40			2.06
O3		1.77, 0.40				2.17
O4	1.03$^{\times 2\rightarrow}$					2.06
O5			1.62, 0.44			2.06
O6				$^{\downarrow \times 2}$ 0.84$^{\times 2\rightarrow}$		1.68
O7			0.93$^{\times 2\rightarrow}$			1.86
O8	1.77, 0.40					2.17
O9	0.83	1.24				2.07
O10			0.55	$^{\downarrow \times 4}$1.10	$^{\downarrow \times 2}$0.31(0.52)^{a}	1.99(2.21)^{a}
O11			1.04$^{\times 2\rightarrow}$			2.08
O12	1.04$^{\times 2\rightarrow}$					2.08
O13		1.05$^{\times 2\rightarrow}$				2.10
O14	1.06$^{\times 2\rightarrow}$					2.12
½O15					0.62(1.05)^{a}	0.62(1.05)^{a}
BVS	6.13	6.13	5.98	6.08	1.24(1.57)^{a}	

Note: M = 0.62 W + 0.38 Mo; As = 0.5 As^{3+} + 0.5□. Bond strengths are calculated as $s = \exp[(R_o - R)/B]$; R_o and B parameters for As, Mo, W are taken from Brown and Altermatt [57], Zocchi [58] and Hong et al. [59], respectively. Values are weighted on the basis of their site occupancy factors.
^a Bond strengths calculated considering ⟨As–O⟩ = 1.77(2) Å as obtained by EXAFS.

with the maximum axis along [001], lies on two symmetry-related, half-occupied sites off-centred in the hexagonal channels at 1.97 Å from two O10 and two half-occupied O15 atoms (see Fig. 1.a,b). The observed offset of As and O15 from the two-fold [100] axis is probably related to the occurrence of the superstructure reflections along [001], as indicated by the TEM investigation (Fig. 2).

A possible ordering scheme could imply an As—□—As—□ sequence (□ stands for vacancy) along [001]. Analogously, a concomitant O15—□—O15—□ pattern should occur, thus forming the typical pyramidal AsO_3 group geometry (Fig. 1.c). This model is in agreement with XANES and EXAFS results (Fig. 3.a, c, d) which indicate that As is present as As^{3+}, bonded to three oxygen atoms at 1.77(2) Å. This value is very close to that reported by Majzlan et al. [49] and Bowell et al. [50], *i.e.* 1.782 Å, who reviewed all As^{3+}-bearing minerals, and seems more realistic than that observed by single-crystal X-ray diffraction (SC-XRD) data (1.97 Å). This is because the latter is likely affected by the "average" character of the obtained structural model. Indeed, the bond valence sum (BVS) on the As atom closely matches the expected value (1.5 for half-occupied As^{3+}) when the distance obtained by EXAFS is considered (Table 6). A quite similar geometry was also observed for As cations in the previously reported (2)-ITB $(As_2O)(MoO_3)_{10}$ compound [24].

Among the M sites, the largest anisotropic displacement ellipsoid, showing an oblate geometry in the (100) plane, is observed for M4 which shares the O10–O10 edge with the AsO_3 group. Nonetheless, the observed high residual electron density peaks are located away from M1, M2 and M3 octahedral cations along [001], suggesting a possible minor deviation of their position in the superstructure with respect to the average model.

A_xWO_3 (with A being H^+, Na^+ or K^+ and *x*-content ≤ 0.3) oxides are known to be mixed-valence compounds, since the insertion of guest cations is charge-balanced by a partial reduction of the W high valence state (+6) into the lower (+5) and/or (+4) states (*e.g.* Refs. [52–55]).

Here, the As^{3+} content observed from both EMPA and SC-XRD data amounts approximately to $0.07-0.08$ atoms per $(W,Mo)O_3$ group. The described compound is therefore likely bearing mixed-valent metal cations. According to XAS data, all W is hexavalent (Fig. 3b), thus implying that Mo is the only mixed-valent metal.

Given the similarity of Mo^{5+}, Mo^{6+} and W^{6+} ionic radii (0.61, 0.59, 0.60 Å, respectively [56]), it is hard to assign a cation distribution among the individual octahedral sites either on the basis of their mean distances ($<M—O> = 1.920$, 1.923, 1.934 and 1.892 Å for M1, M2, M3 and M4 sites, respectively) or their bond-valence sums (6.13, 6.13, 5.98, 6.08 v.u., respectively). Due to the exponential character of the bond strength-bond distance relation, the extremely strong distortion of octahedra (Table 5) is likely the reason of the discrepancies observed for some BVS values (Table 6). The bond valence sum for O6 (1.68 v.u.) is relatively low but not surprising for O-atoms belonging to strongly asymmetric polyhedra. The bond valence sum of the half-occupied O15 (0.62) is actually low but when we consider the average As–O bond distance derived from EXAFS a value close to 1.0 is obtained, which perfectly matches the half-occupancy of this oxygen site.

4. Conclusions

The present study allows the unveiling of an up to now not well-defined member of the (*n*)-ITB family, namely a new (6)-ITB member characterized by an alternation of single HTB slabs and PTB slabs made of six layers of octahedra. To the best of our knowledge, the only previously reported TBO resembling a (6)-ITB phase is the orthorhombic $Sn_4W_{24}O_{76}$ compound described by Steadman et al. [19].

The unit cell of that compound ($a = 50.11$, $b = 7.372$ and $c = 3.895$ Å) is related to the one found for the (6)-ITB studied here via the doubling of the unit cell occurring along [100] rather than along [001]. The structural model they proposed, however, was roughly refined ($R = 19\%$; atomic coordinates not provided) and exhibits some differences with respect to $AsO[(W_{0.62}Mo_{0.38})O_3]_{13}$. The six-octahedra thick PTB slabs

appear similar, even though the stacking of PTB and HTB slabs in AsO $[(W_{0.62}Mo_{0.38})O_3]_{13}$ leads to an alternation along [010] of flattened and regular hexagonal channels where M4 and As occur, respectively (Fig. 1), whereas in $Sn_4W_{24}O_{76}$, a sequence of equally flattened hexagonal channels hosting Sn is realized. Sn atoms appear in fact to be square-coordinated due to the lack of two apical oxygens (O6 of our model). Thus, the TBO studied by Steadman et al. [19] could be more properly described with the structural formula $[Sn_{0.25}(W_{3.0}Sn_{0.25})O_{9.50}\square_{0.25}]_8$.

The present SC-XRD study, supported by the results of the XAS measurements, yielded an orthorhombic average structural model which lacks the long-range order determination for the extra-framework atoms (1 As and 1 O atom located inside the hexagonal tunnel), although a possible ordering scheme along [001] is hypothesized on the basis of the electron diffraction analysis, which clearly shows a doubling of the *c* unit-cell parameter. As a matter of fact, in analogy with what observed for (*n*)-ITB compounds [24,32,34,60], an ordering doubling the *a* unit-cell parameter was expected since the increase of the thickness of the PTB slab with *n* should determine a sequential lengthening of the *a* parameter by ~7.4 Å from lower to upper (*n*)-ITB member. Notwithstanding, no sign of doubling along [100] was observed, either by SC-XRD or ED techniques.

CRediT authorship contribution statement

Meriem Goudjil: Conceptualization, Investigation, Methodology, Software, Writing – original draft. **Giovanni Orazio Lepore:** Methodology, Data curation, Writing – review & editing. **Luca Bindi:** Software, Visualization, Writing – review & editing, Resources, Supervision, Validation. **Enrico Mugnaioli:** Methodology, Software, Visualization, Writing – review & editing. **Tommaso Baroni:** Methodology. **Djillali Mezaoui:** Conceptualization, Methodology. **Paola Bonazzi:** Writing – review & editing, Supervision, Validation.

Declaration of competing interest

The authors declare that they have no known competing financial interests or personal relationships that could have appeared to influence the work reported in this paper.

Data availability

Data will be made available on request.

Appendix A. Supplementary data

Supplementary data to this article can be found online at https://doi.org/10.1016/j.jssc.2023.123987.

References

[1] Y. Xi, Z. Chen, V.G.W. Kiat, L. Huang, H. Cheng, On the mechanism of catalytic hydrogenation of thiophene on hydrogen tungsten bronze, Phys. Chem. Chem. Phys. 17 (15) (2015) 9698–9705.

[2] G. Li, C. Guo, M. Yan, S. Liu, Cs_xWO_3 nanorods: realization of full-spectrum-responsive photocatalytic activities from UV, visible to near-infrared region, Appl. Catal. B Environ. 183 (2016) 142–148.

[3] Y.F. Li, W. Lu, K. Chen, P. Duchesne, A. Jelle, M. Xia, T.E. Wood, U. Ulmer, G.A. Ozin, Cu atoms on nanowire Pd/H_yWO_{3-x} bronzes enhance the solar reverse water gas shift reaction, J. Am. Chem. Soc. 141 (38) (2019) 14991–14996.

[4] D. Delgado, M. Soriano, B. Solsona, S. Zamora, S. Agouram, P. Concepción, J.L. Nieto, Tungsten-titanium mixed oxide bronzes: synthesis, characterization and catalytic behavior in methanol transformation, Appl. Catal. Gen. 582 (2019), 117092.

[5] D. Delgado, P. Concepción, A. Trunschke, J.M.L. Nieto, Tungsten–niobium oxide bronzes: a bulk and surface structural study, Dalton Trans. 49 (38) (2020) 13282–13293.

[6] Y.-L. Shi, M.-P. Zhuo, X.-C. Fang, X.-Q. Zhou, X.-D. Wang, W.-F. Chen, L.-S. Liao, Efficient all-inorganic perovskite light-emitting diodes with cesium tungsten bronze as a hole-transporting layer, J. Phys. Chem. Lett. 11 (18) (2020) 7624–7629.

[7] Z. Sun, X.-G. Sang, Y. Song, D. Guo, D.-Y. Feng, X. Sun, X.-X. Liu, A high performance tungsten bronze electrode in a mixed electrolyte and applications in supercapacitors, Chem. Commun. 55 (95) (2019) 14323–14326.

[8] W.-M. Huang, C.-Y. Hsu, D.-H. Chen, Sodium tungsten oxide nanowires-based all-solid-state flexible transparent supercapacitors with solar thermal enhanced performance, Chem. Eng. J. 431 (2022), 134086.

[9] X.-J. Huang, J. Bao, Y. Han, C.-W. Cui, J.-X. Wang, X.-F. Zeng, J.-F. Chen, Controllable synthesis and evolution mechanism of tungsten bronze nanocrystals with excellent optical performance for energy-saving glass, J. Mater. Chem. C 6 (29) (2018) 7783–7789.

[10] G. Yang, Y. Qi, D. Hu, H. Wang, H. Chen, L. Zhang, C. Cao, B. Liu, F. Xia, Y. Gao, Sodium tungsten bronze (Na_xWO_3)-doped near-infrared-shielding bulk glasses for energy-saving applications, J. Mater. Sci. Technol. 89 (2021) 150–157.

[11] G. Yang, D. Hu, F. Xia, C. Yang, Y. Liu, X. He, Y. Shpotyuk, H. Chen, Y. Gao, Doping sodium tungsten bronze-like ($Na_5W_{14}O_{44}$) near-infrared shielding functional units in bulk borosilicate glasses for energy-saving window applications, Acs Appl. Mater. Inter. 14 (28) (2022) 32206–32217.

[12] G. Hägg, The spinels and the cubic sodium-tungsten bronzes as new examples of structures with vacant lattice points, Nature 135 (3421) (1935) 874.

[13] A. Magnéli, The crystal structure of tetragonal potassium tungsten bronze, Ark. Kemi. 1 (3) (1949) 213–221.

[14] A. Magnéli, R. Mårin, C. Haug, J. Stene, N. Sörensen, Tetragonal tungsten bronzes of degenerated perovskite type, Acta Chem. Scand. 5 (1951) 670–672.

[15] A. Magnéli, G. Andersson, B. Blomberg, L. Kihlborg, Identification of molybdenum and tungsten oxides by X-ray powder patterns, Anal. Chem. 24 (12) (1952) 1998–2000.

[16] A. Magnéli, Studies on the hexagonal tungsten bronzes of-potassium, Acta Chem. Scand. 7 (1953) 315–324.

[17] A. Hussain, L. Kihlborg, Intergrowth tungsten bronzes, Acta Crystallogr. A 32 (4) (1976) 551–557.

[18] A. Hussain, Phase analyses of potassium, rubidium and cesium tungsten bronzes, Acta Chem. Scand. A 32 (1978) 6.

[19] R. Steadman, R. Tilley, I. McColm, A series of orthorhombic tin-tungsten bronzes, J. Solid State Chem. 4 (2) (1972) 199–208.

[20] L. Kihlborg, Chem. Scripta 14 (187) (1978) 79.

[21] M. Parmentier, C. Gleitzer, A. Courtois, J. Protas, Structure cristalline de $Sb_2Mo_{10}O_{31}$, Acta Crystallogr. B 35 (9) (1979) 1963–1967.

[22] C. Rao, J.M. Thomas, Intergrowth structures: the chemistry of solid-solid interfaces, Accounts Chem. Res. 18 (4) (1985) 113–119.

[23] M. Dobson, J. Hutchison, R. Tilley, K. Watts, The structures of intergrowth tungsten bronzes of Ba, Sn, Pb, and Sb, J. Solid State Chem. 71 (1) (1987) 47–60.

[24] M. Goudjil, E. Gutiérrez-Puebla, P. Bonazzi, E. Lunedei, D. Mezaoui, L. Bindi, Synthesis and crystal structure of a series of stoichiometric (*n*)-ITB molybdenum-bronze oxides containing trivalent arsenic, Z. für Kristallogr. - Cryst. Mater. 234 (9) (2019) 569–579.

[25] R. Sharma, L. Kihlborg, Structures and defects of new intergrowth tungsten bronze analogues revealed by high resolution electron microscopy, Mater. Res. Bull. 16 (4) (1981) 377–380.

[26] L. Kihlborg, M. Sundberg, Imaging tunnel atoms in intergrowth tungsten bronzes, Acta Crystallogr., Sect. A: Found. Crystallogr. 44 (6) (1988) 798–805.

[27] L. Kihlborg, M. Sundberg, Inverted twinning in intergrowth tungsten bronzes, Acta Crystallogr. Sect. B Struct. Sci. 53 (1) (1997) 95–101.

[28] L. Kihlborg, H. Blomqvist, M. Sundberg, Low members of the intergrowth tungsten bronze family by partial substitution of molybdenum for tungsten, J. Solid State Chem. 162 (2) (2001) 341–346.

[29] A. Kirkland, J. Sloan, S. Haigh, Ultrahigh resolution imaging of local structural distortions in intergrowth tungsten bronzes, Ultramicroscopy 107 (6–7) (2007) 501–506.

[30] R. Sharma, The relation between structure and composition of intergrowth tungsten bronzoids, Acta Chem. Scand Phys. Inorg. Chem. 39 (6) (1985) 397–403.

[31] R. Sharma, Bronzoid phases in the pseudo-binary system $A_xNb_xW_{1-x}O_3$ with A = K and Cs, Mater. Res. Bull. 20 (11) (1985) 1373–1381.

[32] N. Zakharov, P. Werner, I. Zibrov, V. Filonenko, M. Sundberg, Intergrowth tungsten bronze structures of Pr_xWO_3, formed at 50 kbar: an HRTEM study, J. Solid State Chem. 147 (2) (1999) 536–544.

[33] J.E. Iglesias, A. Castro, R. Enjalbert, J. Galy, Mixed valence oxide $((Sb,As)_2O)Mo_4^{5+}Mo_6^{6+}O_{30}$: synthesis, crystal structure and physical properties, Solid State Sci. 6 (8) (2004) 799–808.

[34] M. Klingstedt, M. Sundberg, L. Eriksson, S. Haigh, A. Kirkland, D. Grüner, A. De Backer, S. Van Aert, O. Terasaki, Exit wave reconstruction from focal series of HRTEM images, single crystal XRD and total energy studies on Sb_xWO_{3+y} ($x \sim$ 0.11), Z. für Kristallogr. - Cryst. Mater. 227 (6) (2012) 341.

[35] CrysAlis, C.C.D. CrysAlis RED, Including ABSPACK Versions 1.171. 32.3. 2006, Oxford Diffraction Ltd, Abingdon, Oxfordshire, England.

[36] G.M. Sheldrick, Includes SHELXS, SHELX and SHELXL-2014, Acta Crystallogr. C 71 (2015) 3–8.

[37] A. Spek, PLATON, an integrated tool for the analysis of the results of a single crystal structure determination, Acta Crystallogr., Sect. A: Found. Crystallogr. 46 (s1) (1990) c34-c34.

[38] J.A. Ibers, W.C. Hamilton, in: James A. Ibers, C. Walter (Eds.), International Tables for X-Ray Crystallography: Revised and Supplementary Tables to Volumes 2 and 3/, Kynoch Press, Hamilton, 1974.

[39] M. Gemmi, E. Mugnaioli, T.E. Gorelik, U. Kolb, L. Palatinus, P. Boullay, S. Hovmöller, J.P. Abrahams, 3D electron diffraction: the nanocrystallography revolution, ACS Cent. Sci. 5 (8) (2019) 1315–1329.

[40] L. Palatinus, P. Brázda, M. Jelínek, J. Hrdá, G. Steciuk, M. Klementová, Specifics of the data processing of precession electron diffraction tomography data and their implementation in the program PETS2. 0, Acta Crystallogr. B: Struct. Sci. Cryst. Eng. Mater. 75 (4) (2019) 512–522.

[41] F. d'Acapito, G.O. Lepore, A. Puri, A. Laloni, F. La Manna, E. Dettona, A. De Luisa, A. Martin, The LISA beamline at ESRF, J. Synchrotron Radiat. 26 (2) (2019) 551–558.

[42] P. Lee, P. Citrin, P.t. Eisenberger, B. Kincaid, Extended x-ray absorption fine structure—its strengths and limitations as a structural tool, Rev. Mod. Phys. 53 (4) (1981) 769.

[43] B. Ravel, M. Newville, ATHENA, ARTEMIS, hephaestus: data analysis for X-ray absorption spectroscopy using IFEFFIT, J. Synchrotron Radiat. 12 (4) (2005) 537–541.

[44] B. Ravel, ATOMS: crystallography for the X-ray absorption spectroscopist, J. Synchrotron Radiat. 8 (2) (2001) 314–316.

[45] A.L. Ankudinov, B. Ravel, J. Rehr, S. Conradson, Real-space multiple-scattering calculation and interpretation of X-ray-absorption near-edge structure, Phys. Rev. B 58 (12) (1998) 7565.

[46] P. Ballirano, A. Maras, Refinement of the crystal structure of arsenolite, As_2O_3, Z. Kristallogr. N. Cryst. Struct. 217 (1) (2002) 177–178.

[47] E. Sevillano, H. Meuth, J. Rehr, Extended x-ray absorption fine structure Debye-Waller factors. I. Monatomic crystals, Phys. Rev. B 20 (12) (1979) 4908.

[48] K. Robinson, G. Gibbs, P. Ribbe, Quadratic elongation: a quantitative measure of distortion in coordination polyhedra, Science 172 (3983) (1971) 567–570.

[49] J. Majzlan, P. Drahota, M. Filippi, Parageneses and crystal chemistry of arsenic minerals, Rev. Mineral. Geochem. 79 (1) (2014) 17–184.

[50] R. Bowell, C. Alpers, H. Jamieson, K. Nordstrom, J. Majzlan, Arsenic: Environmental Geochemistry, Mineralogy, and Microbiology, Walter de Gruyter GmbH & Co KG, 2014.

[51] L.L. George, C. Biagioni, G.O. Lepore, M. Lacalamita, G. Agrosì, G.C. Capitani, E. Bonaccorsi, F. d'Acapito, The speciation of thallium in (Tl, Sb, As)-rich pyrite, Ore Geol. Rev. 107 (2019) 364–380.

[52] B. De Angelis, M. Schiavello, On the interpretation of the X-ray photoelectron spectrum of the $4f$ levels of tungsten in Na_xWO_3 bronzes, Chem. Phys. Lett. 58 (2) (1978) 249–251.

[53] S. Lawrence, S. Stevenson, K. Mavadia, P. Sermon, Solid-state properties of some polycrystalline alkali-metal tungsten bronzes, Proc. Royal Soc. London A. Math. Phys. Sci. 411 (1840) (1987) 95–121.

[54] A. Ramanan, J. Gopalakrishnan, M. Uppal, D. Jefferson, C.N.R. Rao, Bismuth-tungsten oxide bronzes: a study of intergrowth phases and related aspects, Proc. Royal Soc. London A. Math. Phys. Sci. 395 (1808) (1984) 127–139.

[55] J. Besnardiere, B. Ma, A. Torres-Pardo, G. Wallez, H. Kabbour, J.M. González-Calbet, H.J. Von Bardeleben, B. Fleury, V. Buissette, C. Sanchez, Structure and electrochromism of two-dimensional octahedral molecular sieve h'-WO_3, Nat. Commun. 10 (1) (2019) 1–9.

[56] R.D. Shannon, Revised effective ionic radii and systematic studies of interatomic distances in halides and chalcogenides, Acta Crystallogr. Sect. A Cryst. Phys. Diffr. Theor. Gen. Crystallogr. 32 (5) (1976) 751–767.

[57] I. Brown, D. Altermatt, Bond-valence parameters obtained from a systematic analysis of the inorganic crystal structure database, Acta Crystallogr. Sect. B Struct. Sci. 41 (4) (1985) 244–247.

[58] F. Zocchi, Critical comparison of equations correlating valence and length of a chemical bond. Evaluation of the parameters R1 and B for the Mo–O bond in MoO_6 octahedra, Solid State Sci. 2 (3) (2000) 385–389.

[59] Q.-M. Hong, Z.-H. Zhou, S.-Z. Hu, Study on the bond valence parameters for tungsten-oxygen bonds, Hua Hsueh Hsueh Pao B. 62 (2004) 1733–1737.

[60] S. Triantafyllou, P. Christidis, C.B. Lioutas, An X-ray and electron diffraction study of the intergrowth tungsten bronze $Sb_{0.16}WO_3$, J. Solid State Chem. 134 (2) (1997) 344–348.